Journal of Alloys and Compounds 992 (2024) 174560

Contents lists available at ScienceDirect

Journal of Alloys and Compounds

journal homepage: www.elsevier.com/locate/jalcom

Microstructural characterisation and compound formation in rapidly solidified SiGe alloy

Osama Al-Jenabi [a,b,*], Zabeada Aslam [c], Robert F. Cochrane [b], Andrew M. Mullis [b]

[a] School of Mechanical Engineering, University of Leeds, Leeds LS2 9JT, UK
[b] School of Chemical & Process Engineering, University of Leeds, Leeds LS2 9JT, UK
[c] The Bragg Centre for Materials Research, University of Leeds, Leeds LS2 9JT, UK

ARTICLE INFO

Keywords:
Thermoelectric alloy
Nonequilibrium solidification
Rapid quenching
Chemical ordering
Group IV semiconductors

ABSTRACT

Severe Ge segregation to grain boundaries was observed in a Si–14.2 at% Ge thermoelectric alloy rapidly solidified using a drop-tube facility, manifesting itself as a series of regions with uniform stoichiometric compositions. The step change in composition at the interface between adjacent regions was ascribed to the formation of different SiGe pseudocompounds and contradicted the accepted thermodynamic description of the SiGe system as a continuous random solid solution. Rapid solidification increased, rather than decreased, the inhomogeneity degree of the solid product, and the Ge content of the most Ge-rich regions was positively correlated with the cooling rate, which suggested the absence of solute trapping. The transmission electron microscopy/selected area electron diffraction analysis of the most Ge-rich regions revealed superlattice spots indicative of chemical ordering. However, simple chemical ordering within a single diamond cubic unit cell could not explain the fact that most stoichiometries had compositions that were multiples of 5 at% Ge, which indicated the presence of superstructural ordering.

1. Introduction

SiGe alloys are in high demand owing to their extensive use in optoelectronics and the complementary metal-oxide semiconductor (CMOS) technology [1]. Moreover, the recent years have witnessed considerable progress in the use of Si in solar cells [2], SiGe alloys in thermoelectric applications [3], and quantum devices [4]. Considerable attention has been drawn to the applications of $Si_{1-x}Ge_x$ thermoelectric alloys in the electronics industry, mainly because their completely substitutional solid solution structure offers greater flexibility than that of pure Si. These alloys also exhibit high mechanical strength, high melting points, and low thermal conductivity at 900–1200 K and are therefore well suited for use in microelectronics operating at elevated temperatures and thermoelectric power generators [5], [6], [7], [8]. The abundance, nontoxicity, tuneable band gap, and reliability (especially at high temperatures) of these alloys enable operation in harsh environments, such as those encountered during heat recovery in the steel industry [7], [8], [9], [10], [11].

The realisation of optimal thermoelectric performance relies on the establishment of a highly homogeneous SiGe microstructure with minimal compositional variation. However, this goal is difficult to realise because of the wide separation between the liquidus and solidus curves of the constituent elements and variations in their densities, lattice parameters, and melting temperatures [7], [8], [12]. Unlike typical alloys, homogeneous SiGe alloys with the desired stoichiometries are challenging to prepare because of the substantial miscibility gap between the solid solutions of Si and Ge [8]. The equilibrium SiGe phase diagram (Fig. 1) reveals that a simple near-ideal solid solution is observed over the entire composition range, suggesting that equilibrium solidification should induce the strong partitioning of Ge to grain boundaries and thus result in a highly inhomogeneous microstructure. Scheil equation–based calculations [7] indicate that this partitioning can result in the formation of almost pure Ge at grain boundaries, with the associated side-effects including increased phonon scattering and localised heating. The above results demonstrate that homogenous and refined microstructures can potentially be realised via rapid solidification.

In general, the band gap and thermoelectric performance of semiconducting alloys can be controlled or modified by composition tuning, e.g. a shift to more Ge-lean compositions in SiGe alloys may reduce thermal conductivity by increasing phonon scattering [3], [7]. However, given the high cost of Ge, the Ge content of SiGe alloys should be decreased [3]. Rapid solidification is a viable strategy for overcoming

* Corresponding author at: School of Mechanical Engineering, University of Leeds, Leeds LS2 9JT, UK.
E-mail address: mnoij@leeds.ac.uk (O. Al-Jenabi).

https://doi.org/10.1016/j.jallcom.2024.174560
Received 14 February 2024; Received in revised form 13 April 2024; Accepted 19 April 2024
Available online 21 April 2024

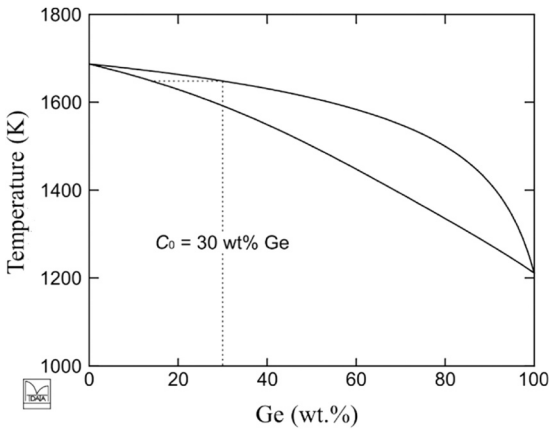

Fig. 1. SiGe equilibrium phase diagram.

the challenges in the production of new classes of SiGe thermoelectric alloys by reducing their Ge content without compromising thermoelectric performance [7], [13], [14]. However, research on $Si_{1-x}Ge_x$ alloys, especially that dealing with partitioning and compound formation, is limited. Previous studies have shown that homogeneous melts can be produced by rapid cooling during microgravity processing, with the absence of thermal convection and density-based segregation enabling the formation of more compositionally uniform structurer [14]. Zhang, et al. [15] used melt spinning to investigate the effect of cooling rate ($>10^5$ K s^{-1}) on the microstructure of n-type SiGe alloys. The results of energy-dispersive X-ray spectroscopy (EDX) point measurements suggested that inhomogeneity was caused by near-equilibrium solidification. Rapid solidification decreased grain size and reduced (but did not fully supress) inhomogeneity.

Rapid cooling reduces segregation, probably by inducing solute trapping, and can increase homogeneity and promote grain refinement. Nagai, et al. [14] compared conventionally processed SiGe alloys with those processed under microgravity conditions using the Japan Microgravity Center's (JAMIC's) drop shaft and a 10 m drop-tube. The former samples had large (diameter ≈ 0.2 mm) grains and featured severe segregation, whereas the latter exhibited reduced (but not completely eliminated) segregation, which was ascribed to diffusion along the solid–liquid interface during unidirectional solidification.

Panofen and Herlach [16] used high-speed videography to study growth in SiGe alloys containerlessly processed using electromagnetic levitation. For a Si–2.5 at% Ge alloy, planar growth resulting in coarse elongated grains was observed at low undercooling, whereas faceted dendritic growth giving rise to a fine-grained microstructure was observed under the conditions of high undercooling. Contrary to the authors' expectations, the samples solidified from the surface to the centre, which resulted in higher Ge content at the centre. Herlach, et al. [17] studied the crystallisation of $Ge_{25}Si_{75}$, $Ge_{50}Si_{50}$, and $Ge_{75}Si_{25}$ alloys using a containerless levitation technique, showing that growth kinetics were similarly affected by undercooling. At a lower critical undercooling, the first transition was from faceted to dendritic growth, whereas at a higher critical undercooling, a transition from dendritic to planar growth was observed. The high-undercooling transition occurred at temperatures of 200–260 K for all compositions, with slightly higher values observed for dilute alloys, and the lowest value observed for the equimolar composition. Numerous microstructural morphologies, from faceted twin structures at an undercooling of 180 K to coarse grains with dendrite segregation at an undercooling of 316 K, were observed in a Ge–1 at% Si alloy processed by electromagnetic levitation. At an undercooling of 373 K, the microstructure was segregation-free and refined into an equiaxed structure [18]. Similarly, the application of electromagnetic levitation to the processing of pure Ge resulted in a transition from lateral to continuous growth in a highly undercooled (≥400 K) liquid [19], although this critical temperature could be considerably lowered by the addition of solutes at very low concentrations (<100 ppm) [20]. In melt spinning experiments, the refinement of grain size to <5 μm by rapid solidification reduced thermal conductivity by 20–30% [15].

Hussain, et al. [7] subjected a Si–30 wt% Ge alloy to cooling at rates of 1800–20,000 K s^{-1} via drop-tube processing. Contrary to the authors' expectations, the degree of segregation and heterogeneity increased with the increasing cooling rate, and compound-like regions with preferred stoichiometries were observed in Ge-rich grain-boundary regions. The observation of stoichiometric compositions at grain boundaries agreed with previous works on SiGe alloys prepared by melt spinning [15]. Moreover, other authors [21,22] observed preferred stoichiometries in ball-milled SiGe powders.

Hussain, et al. [7] used transmission electron microscopy (TEM)/-selected area electron diffraction (SAED) analysis to search for chemical ordering in the stoichiometric regions identified at the Ge-rich grain boundaries, albeit with no success. However, such ordering may be possible, e.g. Duda, et al. [23] performed nonequilibrium molecular dynamics simulations to show that atomic ordering can control thermal conductivity in semiconductor alloys used for low-temperature applications.

In contrast to most other alloys, rapidly solidified SiGe alloys exhibit increased heterogeneity, which, however, does not contribute to improved thermoelectric performance. Consequently, the present study does not deal with thermoelectric property characterisation but rather examines compound formation and inhomogeneous microstructural evolution during the rapid solidification of a thermoelectric Si–14.2 at% Ge (30 wt% Ge) alloy rapidly solidified using a drop-tube facility.

2. Experimental

2.1. Powder fabrication using the drop-tube technique

The as-cast $Si_{70}Ge_{30}$ alloy (4.2 g) was melted and sprayed using a 6.5 m high-vacuum drop-tube to produce powders with particle sizes from >850 to <38 μm. This technique permits both rapid cooling and (as the sample is in free-fall) containerless processing, thus enabling deep undercooling [24]. The drop-tube facility [7] was filled with nitrogen gas to protect the molten sample from oxidation.

A pre-alloyed $Si_{70}Ge_{30}$ alloy (Si–14.2 at% Ge) was sourced from Goodfellow as solid lumps, which were crushed into small pieces (total mass ≈ 4.2 g) to fit into the drop-tube crucible. The base of this crucible had three 300 μm–diameter laser-drilled holes enabling melt ejection upon pressurisation. The crucible and a graphite susceptor (used to aid heating) were placed inside a twin-walled alumina heat shield, and the assembly was centred inside an induction heating coil connected to a 3-kW radiofrequency generator at the top of the drop-tube. During melting, an R-type thermocouple was used to record the temperature within the crucible.

The drop-tube was evacuated by two-stage pumping. First, a rotary vane pump was used to reach a pressure of 6.8×10^{-3} mbar, and the tube was then flushed with N_2 at a pressure of 480 mbar. The pump-flush cycle was repeated three times. Second, a turbomolecular pump was used to reach a pressure of $<2 \times 10^{-5}$ mbar, and the tube was refilled with N_2 to 480 mbar. The melt was sprayed into the thus established oxygen- and moisture-free atmosphere by pressurising the crucible to 4 bar with N_2 gas. To ensure full melting, a superheating of ~50 K was applied, with the total heating cycle lasting 130 min. After cooling, the powders were collected from a catch-pot at the bottom of the drop-tube and sieved to afford eight standard size fractions (droplet diameter = 75–53, 106–75, 150–106, 212–150, 300–212, 500–300, 850–500, and >850 μm). The residue in the crucible remaining after the melt ejection was used as a close-to-equilibrium reference sample, as the cooling rate of this residue (0.172 K s^{-1}, or 10 K min^{-1}) was precisely known because of the controlled cooling of the drop-tube furnace after the

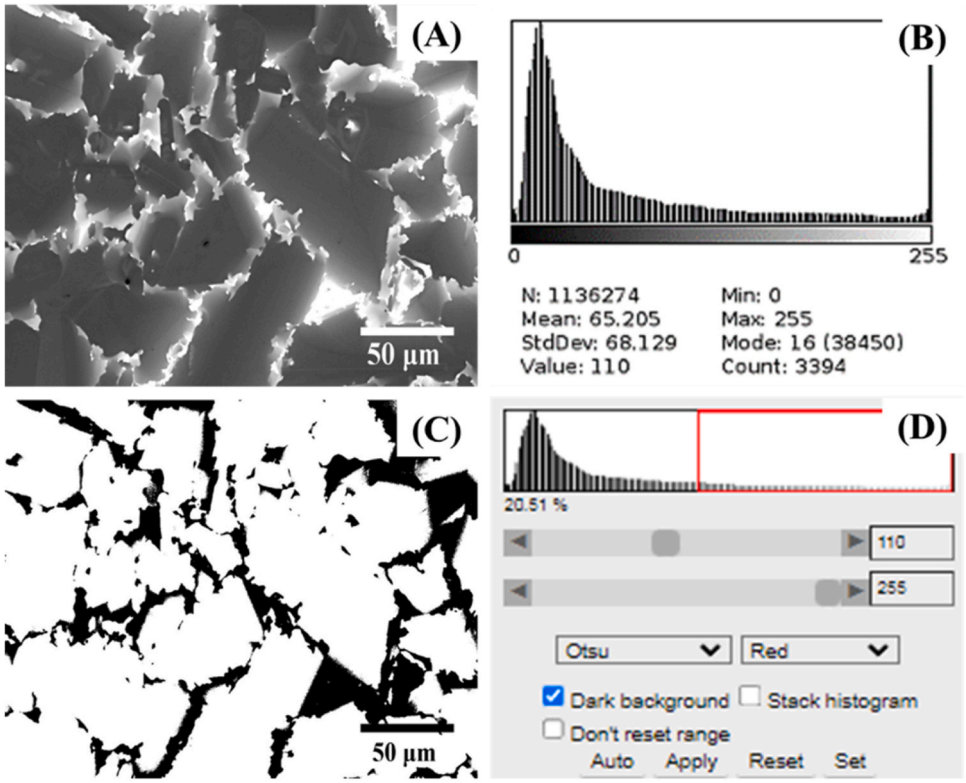

Fig. 2. ImageJ-based analysis of a scanning electron microscopy (SEM) backscatter image of rapidly solidified $Si_{70}Ge_{30}$ droplets (>850-µm fraction). (A) SEM backscatter image, (B) histogram of intensities for the normalised image, (C) binary image obtained by image thresholding, and (D) illustration of Otsu's analytical method used for automatic image thresholding, showing a region quantitatively identified and used as a threshold for greyscaling (110–255). The analysis was repeated for greyscaling in the ranges of 100–255 and 105–255.

ejection. EDX was used to confirm that all samples (i.e., the residue, bulk material, and drop-tube powders) were of the same nominal composition.

2.2. Characterisation techniques

The samples were cold-mounted, ground using SiC grinding papers in the order P240, P600, and P1200, and polished with diamond paste in the order of 6, 3, and 1 µm. Optical microscopy (Olympus BX51) was used to ensure an appropriate surface finish at each grinding/polishing stage before moving on to the next (finer) grade. For scanning electron microscopy (SEM), the final polishing was performed for 5 min using a 0.1-µm colloidal silica suspension (Buehler Automet 250 automatic polishing machine) at a force of 20 N, base rotation speed of 140 rpm, and head rotation speed of 50 rpm. Microstructure and composition were probed by SEM (Hitachi SU8230) coupled with EDX (Oxford Instruments Aztec Energy). A photodiode backscattered electron detector was used to obtain backscatter images, wherein the sufficient contrast obtained because of the high Si/Ge ratio negated the need for sample etching. Low- and high-resolution imaging were performed at accelerating voltages of 20 and 5 kV, respectively; in addition, a probe current of 30 µA and appropriate magnification were selected for each size fraction. EDX point measurements and line scans across the grain boundaries were used for quantitative composition analysis.

X-ray diffraction (XRD) patterns were recorded in the 2θ range of 20–100° on a Bruker D8 X-ray diffractometer using Cu K_α radiation (λ = 1.54056 Å) collimated through a 1 mm–wide rectangular opening. For initial peak determination, the XRD patterns were acquired at 2θ = 20–100°, step size = 0.033°, and scan time = 40 min. To enhance the resolution of the XRD peaks, six individual scans per sample were performed at a smaller step size of 0.01649° and longer scan time of 2 hr, with each scan covering a range of 5° around the approximate peak locations (25–30°, 45–50°, 53–58°, 67–72°, 73–78°, and 85–90°) determined in the initial scan. As Si and Ge have different lattice parameters and form a continuous solid solution, we assumed that the local compositions could be quantitatively determined using Vegard's law.

The residual SiGe and rapidly solidified powders (>850- and 150–106-µm fractions) were subjected to focused-ion-beam milling and examined by TEM to investigate the effects of the rapid solidification on the Ge content variation across grain boundaries and chemical ordering. An FEI Helios G4 FEGSEM instrument was used to focus a high-energy beam of Ga^+ ions, section the area of interest, and weld it onto a Cu TEM grid. The ion beam was then used to slice the 12 µm × 8 µm sample to a thickness of <100 nm.

The residual and rapidly solidified samples were probed by bright-field TEM imaging, EDX line scanning and mapping, and SAED pattern analysis using an FEI Titan Themis microscope operating at 300 kV. A Gatan OneView CMOS digital camera (16 megapixel) was used to acquire bright-field images. A Super-X EDX system based on a windowless four-detector design was used in conjunction with the Velox 2.4 software. The SAED patterns of Ge-rich, intermediate, and Si-rich regions were indexed using ICDD crystallographic data files (references 01–071–4636, 04–008–2206, and 04–006–2527, respectively) and the SingleCrystal software.

2.3. Image processing

The open-source ImageJ software was used for SEM image analysis to determine the volume fractions of the Ge-rich grain-boundary material and Si-rich grains. Fig. 2(A) shows a typical SEM image (>850-µm fraction) processed to improve the signal-to-noise ratio by smoothing the edges and normalising the background to achieve better contrast for distinguishing between Si-rich and Ge-rich regions.

Fig. 2(B) shows the grey level histogram for the resulting image.

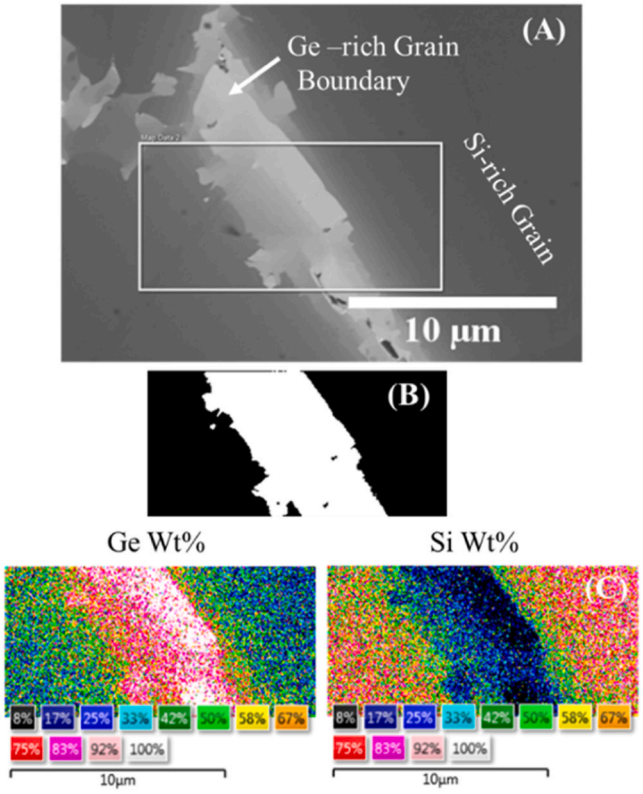

Fig. 3. Check performed with energy-dispersive X-ray spectroscopy (EDX) map to verify the performance of Otsu's thresholding. (A) SEM backscatter image, (B) Otsu's thresholding image, and (C) EDX map.

Table 1
Parameters of the heat-transfer model used to calculate the cooling rate of the rapidly solidified $Si_{70}Ge_{30}$ alloy droplets.

Material	Parameter	Value
N_2 [24]	Specific heat capacity, C_{pg}	1039 J kg^{-1} K^{-1}
	Thermal conductivity, K_g	2.6×10^{-2} W m^{-1} K^{-1}
	Kinematic viscosity, μ	1.78×10^{-5} N s m^{-2}
	Density, ρ_g	1.16 kg m^{-3} (at 0.1 MPa)
	Molar gas constant, R	8.314 J mol^{-1} K^{-1}
$Si_{70}Ge_{30}$	Specific heat capacity, C_p	6.55×10^{2} J kg^{-1} K^{-1}
	Latent heat of fusion, L	1.62×10^{6} J kg^{-1}
	Density, ρ	2.75×10^{3} kg m^{-3}
	Emissivity, ε	0.26
		$\varepsilon_{Si} = 0.27$ [25], $\varepsilon_{Ge} = 0.217$ [26]

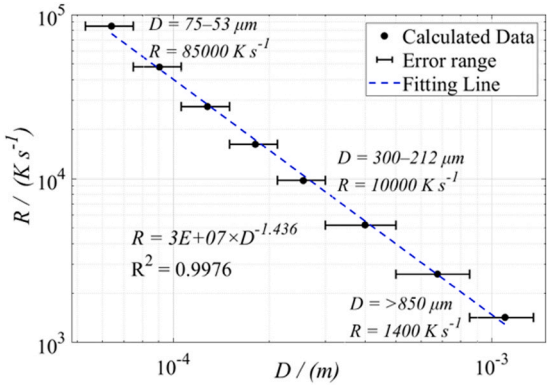

Fig. 4. Cooling rates (R) estimated for different droplet diameters (D).

From this histogram, the grey level marking the threshold between the Si-rich grains and Ge-rich grain boundaries was determined as 105 ± 5 (on the standard 0–255 grey-level scale). Next, Otsu's method was used for automatic thresholding to afford a binary image (Fig. 2(C, D)) delineated into grains and grain-boundary regions. The volume fractions of these regions were obtained from the black/white pixel ratio, and the error limits on the threshold were used to estimate the error bars on the volume fractions of the two phases. Fig. 3 shows the correspondence between the boundaries picked using image processing and the step change in concentration picked using EDX mapping, revealing a strong correlation between the black-to-white transition in the Otsu's image shown in Fig. 3(B) with the Ge concentration step in the EDX map shown in Fig. 3(C). Comparison of the backscatter image shown in Fig. 3(A) with the EDX images shown in Fig. 3(C) reveals that the step change in backscatter contrast corresponds to a step change in composition, which enables unambiguous discrimination between Si-rich grains and Ge-rich grain boundaries. Three SEM backscatter images were analysed for each size fraction, bulk material, and crucible residue.

3. RESULTS

3.1. Cooling rate determination for drop-tube-processed alloy

A heat-transfer model based on thermal flux balance was used to estimate the cooling rate of free-fall droplets of different sizes [24]. In a free-fall scenario, precooled droplets exist in a static N_2 atmosphere and therefore feature negligible thermal gradients. Based on the SiGe phase diagram (Fig. 1), the liquidus and solidus temperatures of the examined alloy (14.2 at% Ge) were determined as 1661 and 1596 K, respectively, corresponding to a melting interval of 65 K. The thermophysical properties of the alloy required to estimate the cooling rate, including specific heat capacity (C_p), latent heat of melting (L), liquid density (ρ), and surface emissivity of the melt (ε), were calculated as the composition-weighted averages of the values for elemental Si and Ge. The parameters used in the model are given in Table 1. Fig. 4 presents the cooling rates calculated using the heat-transfer model for the >850-, 300–212-, and 75–53-µm fractions. The corresponding terminal velocities in the drop-tube ranged from ~1.5 m s^{-1} for the 75–53-µm fraction to ~8 m s^{-1} for the >850-µm fraction. Notably, the cooling rate was well approximated by a power-law fit.

3.2. SEM backscatter imaging

To confirm the nominal composition of the starting alloy, we performed EDX area scans over the entire field of view of the corresponding backscatter images. The results of measurements performed at eight sites showed that the experimental mean composition was identical to the nominal composition within ±0.6 wt%, consistent with the experimental error of EDX measurements.

SEM backscatter imaging was used to characterise the microstructure of the reference sample, namely bulk $Si_{70}Ge_{30}$, and achieved a good contrast in the atomic number. The observed microstructure (Fig. 5(A)) agreed with that expected from the phase diagram, featuring large Si-rich grains (dark) surrounded by localised Ge-rich grain boundaries (bright). This structure indicated the occurrence of extensive solute segregation during solidification, consistent with previous findings [7, 14,15]. The extent of this segregation was probed by performing point EDX measurements in Si- and Ge-rich regions, and the results were compared with those obtained for the crucible residue (Fig. 5(B)). The grain size of the crucible residue exceeded that of the starting material; apparently, the grain-boundary regions occupied a smaller fraction of the sample than starting material but were more Ge-rich.

Fig. 6 shows the microstructure of a typical droplet (500–300-µm fraction) cooled at an estimated rate of 4200–8400 K s^{-1}. This microstructure (and those of droplets with other sizes) was qualitatively similar to those of the starting material and crucible residue, featuring

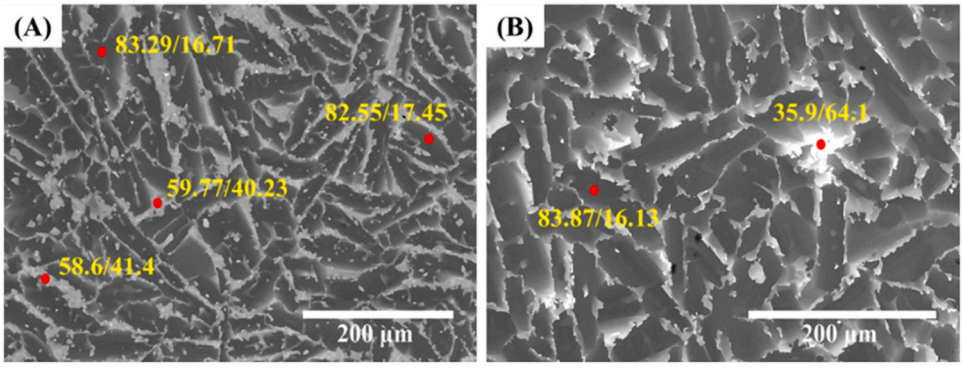

Fig. 5. SEM backscatter images of (A) the starting alloy and (B) crucible residue. Red dots indicate the locations of point EDX measurements, and the corresponding compositions are presented in yellow as Si (wt%)/Ge (wt%).

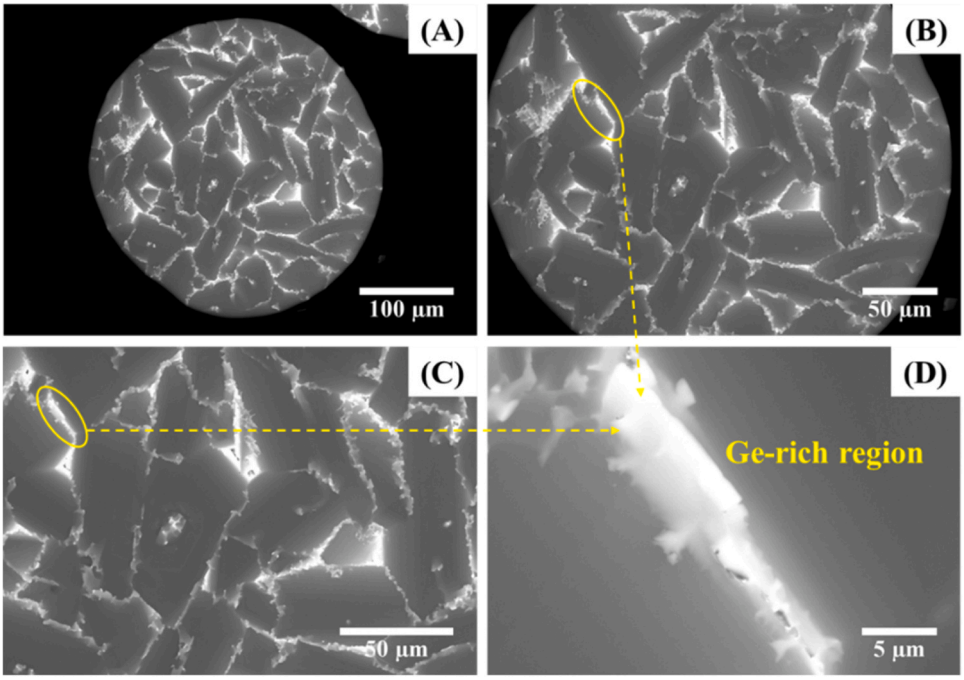

Fig. 6. (A, B) SEM backscatter images of $Si_{70}Ge_{30}$ droplets with diameters of 500–300-µm showing droplet morphology. (C) High-magnification backscatter image displaying the appearance of small distinct Ge-rich grain boundaries and considerably larger Si-rich grains. (D) High-magnification backscatter image displaying distinct Ge-rich grain boundaries (yellow oval).

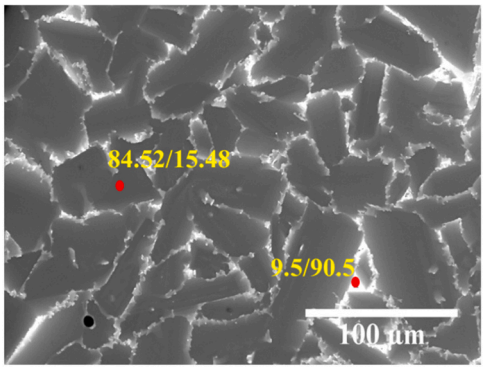

Fig. 7. SEM backscatter image of $Si_{70}Ge_{30}$ droplets with diameters of 500–300-µm with the results of EDX point measurements.

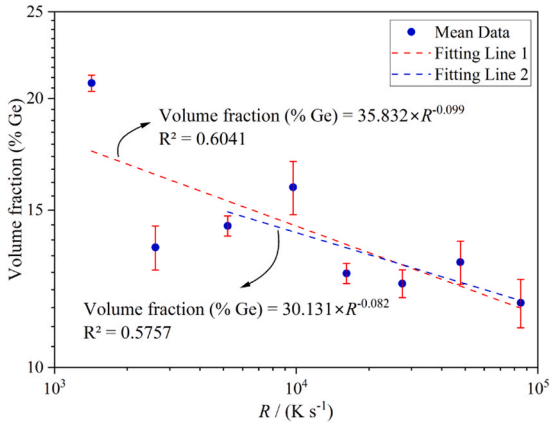

Fig. 8. Mean volume fraction of the Ge-rich material (%) as a function of cooling rate.

Table 2
Calculated mean Ge contents of the grain-boundary regions.

Cooling rate, R/K s^{-1}	Volume fraction of grain-boundary region, V_{GB}/%	Grain density, ρ/g cm^{-3}	Density of grain-boundary region, ρ_{GB}/g cm^{-3}	Mass fraction of grain-boundary region, M_{GB}/%	Content of grain-boundary region, C_{GB}/wt%
-	37.21 ± 2.58	2.81	3.53	57.53	40.20
0.172	15.92 ± 0.70	2.81	4.19	30.20	62.31
1424	20.80 ± 0.43	2.77	3.98	37.51	55.22
2615	13.63 ± 0.77	2.77	4.49	26.50	72.11
5211	14.40 ± 0.37	2.77	4.42	27.77	69.70
9719	15.91 ± 1.09	2.77	4.29	30.19	65.47
16163	12.74 ± 0.33	2.77	4.61	25.02	76.15
27480	12.41 ± 0.44	2.76	4.66	24.46	77.75
47793	13.11 ± 0.72	2.76	4.58	25.64	75.03
84911	11.81 ± 0.72	2.76	4.75	23.43	80.95

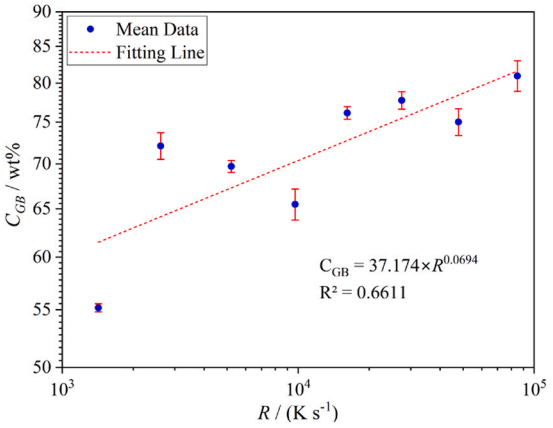

Fig. 9. Calculated Ge content of the grain-boundary material as a function of cooling rate.

dark Si-rich grains surrounded by bright Ge-rich grain boundaries. However, the results of EDX point measurements (Fig. 7(A)) indicated that the partitioning in the rapidly cooled samples considerably exceeded that in the starting alloy and crucible residue. In particular, the Ge content of the Si-rich grains was relatively consistent at 15–17 wt%, whereas that of the grain-boundary regions increased from 64 wt% in the crucible residue to >90 wt% in the drop-tube samples. This behaviour was the opposite of that expected for rapid solidification, as solute trapping was expected to reduce these concentration gradients. In fact, the value of the drop-tube samples was closer to that obtained using the Scheil equation [7], which predicted the formation of nearly pure Ge at the end of the solidification in the droplets but not in the starting material or the crucible residue. This finding cannot be ascribed to an instrumental artefact, as scale refinement in the drop-tube sample would lead to an EDX interaction volume that was more (and not less) conducive to the sampling of adjacent Si-rich grains during the determination of the Ge content at the grain boundaries.

The SEM images indicated a number of unexpected features, which are flagged here for further investigation in the following sections. First, the volume fraction of the Ge-rich grain-boundary material decreased with the increasing cooling rate; second, areas with discrete grey levels separated by step composition changes were observed (e.g., Fig. 6(D)).

Owing to very clear delineation between the Si-rich grains and Ge-rich grain boundaries, the first of these questions may be addressed by quantitative image processing, as outlined in Section ↱2.3. Fig. 8 shows the effects of the cooling rate on the volume fraction of the Ge-rich material, showing two trend lines, one obtained considering all points, and the other obtained considering the six points on the right-hand side of the figure, i.e., those with the highest cooling rate. Lower cooling rates were expected to result in a coarser microstructure and higher scatter in the results of image processing, as confirmed by the large deviations of the two leftmost points from the trendlines. Hence, both lines were similar, which allowed us to claim that the cooling rate was weakly correlated with the volume fraction of the Ge-rich material. However, a very significant difference was observed between the starting material (volume fraction of the Ge-rich material = 37.21%, not shown in the plot because of the unknown cooling rate) and drop-tube-cooled powders (volume fraction of the Ge-rich material = 12.5–21.5%). Given that the composition of the alloy was fixed, the smaller volume fraction of the Ge-rich material suggested that (i) the bulk grains had a higher Ge content, whereby less Ge was available for migration to the grain boundaries and/or (ii) the Ge content of the grain boundaries was higher. The latter possibility was consistent with the literature [7] and results of point EDX measurements given above, which also suggested that the Ge content of the Si-rich grains decreased (and not increased) with the increasing cooling rate.

3.3. Mass-balance calculation

Given that an iterative calculation was performed to realise a self-consistent conversion from the volume fraction of the Ge-rich material to its mass fraction, the composition of the Ge-rich material was determined using a mass-balance calculation. The grain-boundary volume, V_{GB}, was determined by image analysis (Fig. 8), and densities were estimated based upon composition. The iteration to achieve a self-consistent solution was performed between the Ge content of the grain-boundary region (C_{GB}) and the density of the grain-boundary material (ρ_{GB}). Table 2 lists the data for the self-consistent solution, and Fig. 9 presents a plot of C_{GB} versus the cooling rate, revealing a weak correlation between these parameters.

3.4. SEM-EDX line scan analysis

The presence of discrete grey areas in the backscatter images suggested the possibility of discrete compositions, which was explored further using EDX, as illustrated below for the 500–300-μm fraction. A scanned area was selected to investigate the transition between the Si- and Ge-rich regions. Fig. 10 displays the selected region alongside the EDX-determined variations in Si and Ge contents along the indicated transect, revealing step changes corresponding to the discrete grey areas. Four greyscale levels can be identified, with a Si-rich grain boundary on the left transitioning to the Ge-rich grain boundary at ~9 μm. Beyond a distance of ~11.5 μm, a gradual transition is observed, with the Si content eventually plateauing to a constant value.

Fig. 10(B) presents the results of EDX line scan analysis conducted along the transect shown in Fig. 10(A), showing the presence of Si-rich regions (~85 wt% Si) on the left and right sides. This finding was consistent with the results of EDX point measurements in Fig. 7. At 11.5–20 μm, a gradual transition with no evidence of step change in contrast was observed. However, at ~9 μm, a step-like transition from a Ge content of ~15 wt% to that of ~60 wt% was observed, occurring over a distance of <0.5 μm, although this distance may reflect the interaction volume of the EDX probe, wherein the boundary could be sharp. This behaviour differed from that predicted by the Scheil equation, both with regard to the step-like change in the Ge content and the fact that the Ge content within the grain-boundary region plateaued at

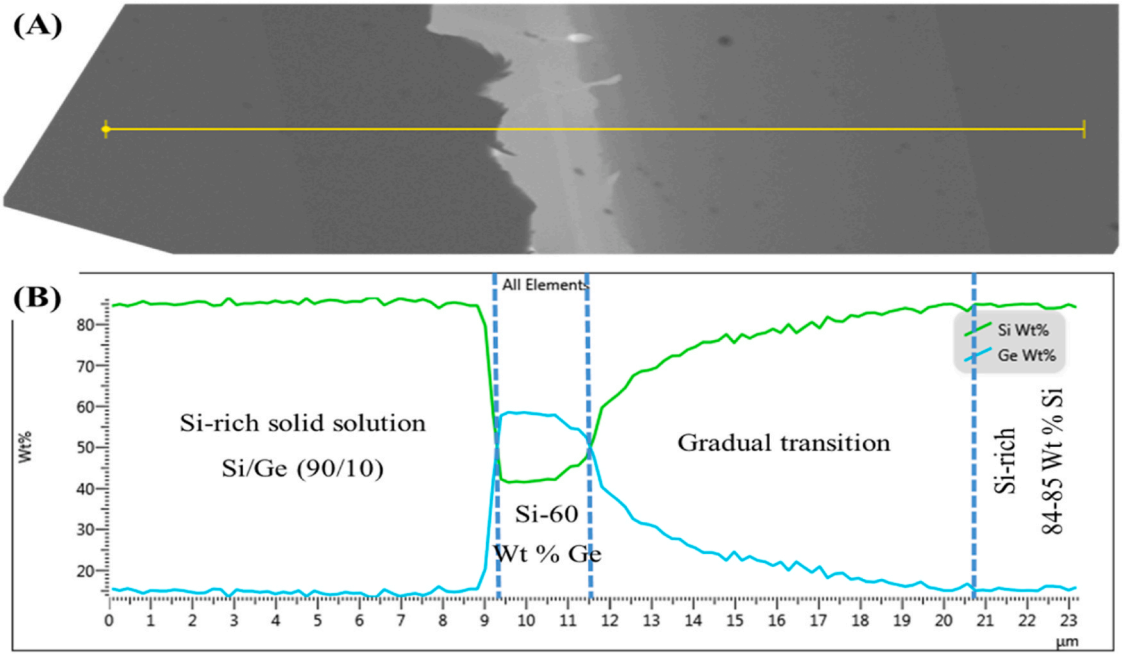

Fig. 10. SEM-EDX analysis of a rapidly solidified $Si_{70}Ge_{30}$ particle (500–300-μm fraction). (A) SEM image (yellow line indicates the line scan direction) and (B) changes in Si and Ge contents along the transect in (A).

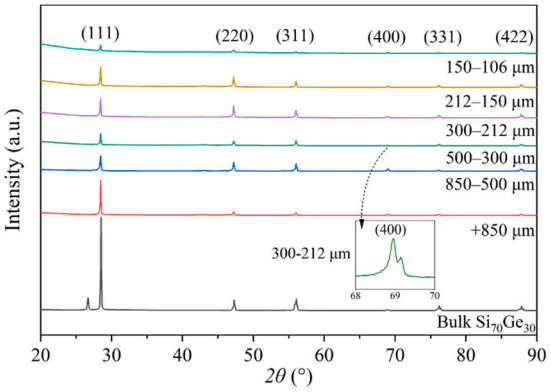

Fig. 11. X-ray diffraction patterns of the rapidly solidified $Si_{70}Ge_{30}$ droplets with different diameters. Inset: Expansion around the (400) peak of the 300–212-μm fraction.

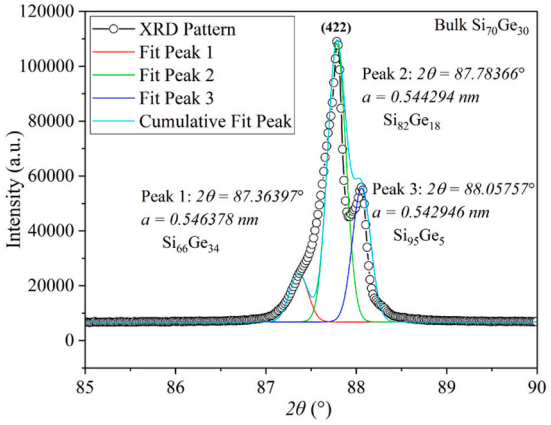

Fig. 12. Gaussian fitting–deconvoluted (422) peak of the bulk $Si_{70}Ge_{30}$ alloy.

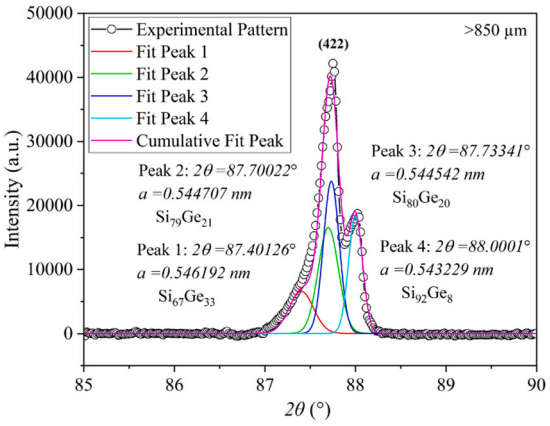

Fig. 13. Gaussian fitting–deconvoluted (422) peak of the >850-μm fraction.

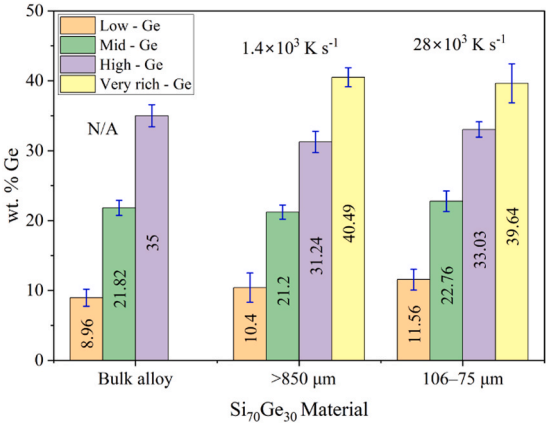

Fig. 14. Relative contributions of fractions with different Ge contents in bulk and rapidly cooled samples (N/A = cooling rate not known).

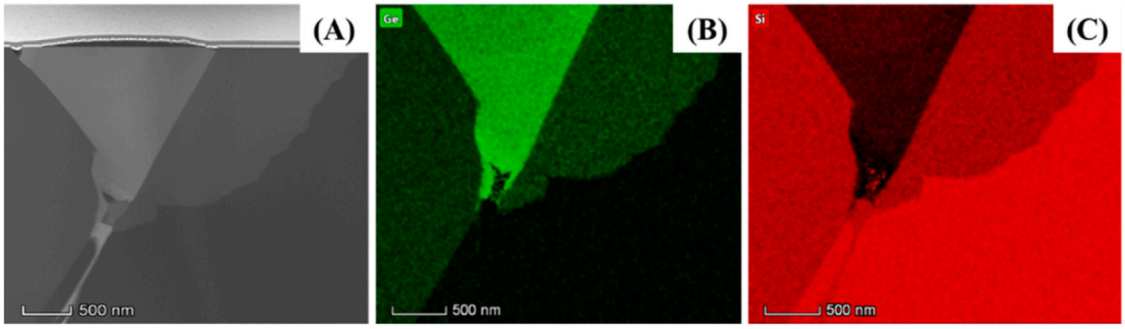

Fig. 15. (A) Bright-field transmission electron microscopy (TEM) image and (B) Ge and (C) Si distributions of the >850-μm fraction showing four distinct stoichiometric regions. Note: the magnification is consistent across all three maps, while the field of view is not.

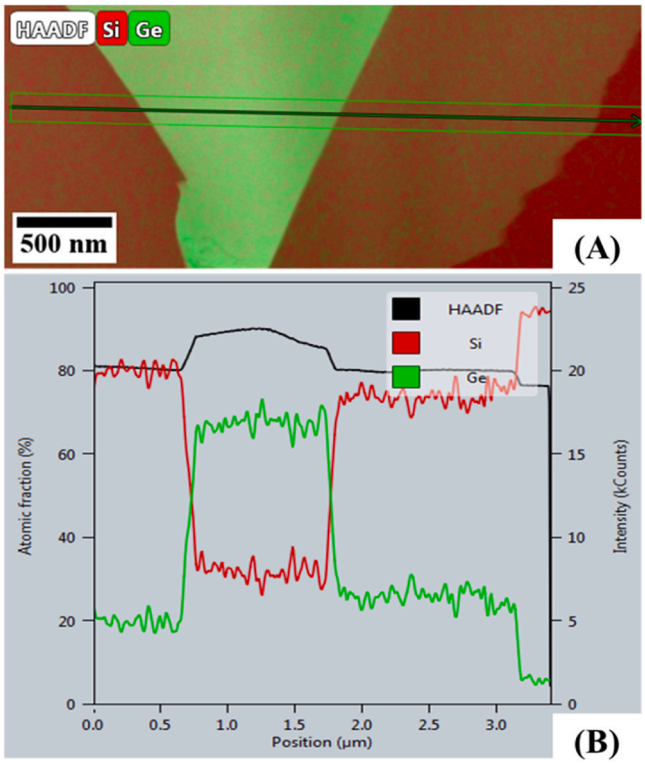

Fig. 16. (A) TEM/EDX map of >850-μm fraction showing distinct stoichiometric regions and the line scan trajectory. (B) Elemental composition along the indicated trajectory.

~60 wt% rather than continuing to increase.

3.5. XRD analysis

As the lattice parameter of pure Si (a_{Si} = 0.54309 nm) differs from that of pure Ge (a_{Ge} = 0.56580 nm) [27], a Vegard's law plot can be used to estimate the composition of a SiGe solid solution from the measured peak positions. However, we observed a small systematic shift in the measured peak positions, which, as expected, was more pronounced for small-angle peaks. Therefore, to improve accuracy, the values of lattice constants (a_{SiGe}, a_{Si}, and a_{Ge}) were determined for each reflection with a separate application of Vegard's law in each case.

The XRD pattern of bulk $Si_{70}Ge_{30}$ featured seven main peaks (Fig. 11), one of which ($2\theta = 26°$) could not be indexed to either Si or Ge and was not observed for drop-tube powders, thus probably indicating the oxidation of the starting material upon storage and handling in air. The splitting of the (311) peak suggested a composite peak with different subpeaks corresponding to different compositions. As described in the Experimental Section, to resolve these composite peaks with greater fidelity, we scanned them separately within a range of $2\theta = 5°$ approximately centred on the known peak position. Peak splitting should be more evident at high 2θ because of the greater peak separation but may be masked by the lower peak intensity.

Fig. 12 shows the (422) peak deconvoluted using Gaussian fitting (OriginPro) into the signals of low-Ge (5–11 wt%), mid-Ge (18–25 wt %), and high-Ge (31–37 wt%) materials with average contributions ± standard errors of 8.98 ± 1.23 wt%, 21.82 ± 1.07 wt%, and 35.06 ± 1.57 wt%, respectively. Despite EDX indicating the presence of a Ge-rich material containing >40 wt% Ge, no evidence of this was found in the XRD data, presumably because of the small volume fraction of this material. Tayebi et. al. [21] and Zamanipour et al. [22] claimed that the composition of SiGe compounds cannot be determined by XRD because of the inability of this technique to resolve such split peaks. However, this appears not to be the case here. Interestingly, this finding was consistent with the observations made for the drop-tube samples, as exemplified by the deconvoluted (422) peak of the >850 μm sample (Fig. 13). Fig. 14 shows the contents of low-, medium-, and high-Ge materials in the bulk alloy, revealing that this grouping can be applied even when one of three peaks has not been resolved. However, this is not appropriate in the case of four peaks (e.g. (400) and (422) for the >850- and 106–75-μm fractions). For instance, in the case of the >850-μm fraction, four compositions may arise, namely low-Ge (7–15 wt%), mid-Ge (16–23 wt%), high-Ge (28–35 wt%), and very Ge-rich (38–44 wt%), with the corresponding average contributions ± standard errors equalling 10.40 ± 2.09 wt%, 21.20 ± 1.01 wt%, 31.24 ± 1.53 wt%, and 40.49 ± 1.36 wt%, respectively.

Given that the Si- and Ge-rich regions can have different thermal expansion coefficients, rapid cooling may induce strain, the influence of which should also be considered. However, XRD analysis has been confined to the study of the effect of composition on lattice parameters and, hence, peak positions. In the case of a well-defined unidirectional strain and single-crystalline sample, this may lead to peak shifting and confusion with the effects of composition. However, this is not the case here, as the examined polycrystalline samples are expected to have randomly oriented strains that are more likely to result in peak broadening with no net shift of peak position [28]. Conversely, in the situation studied by Shah, et al. [29], a peak shift was observed for a SiGe thin film.

3.6. TEM imaging and TEM/EDX analysis

The crucible residue and two rapidly solidified samples, namely the >850- and 150–106-μm fractions, were subjected to TEM/EDX analysis. Fig. 15 shows a representative microstructure of the Ge-rich grain-boundary region of the >850-μm fraction. The corresponding bright-field TEM image (Fig. 15(A)) shows several step changes in contrast, with the corresponding Ge and Si mappings presented in Fig. 15(B) and

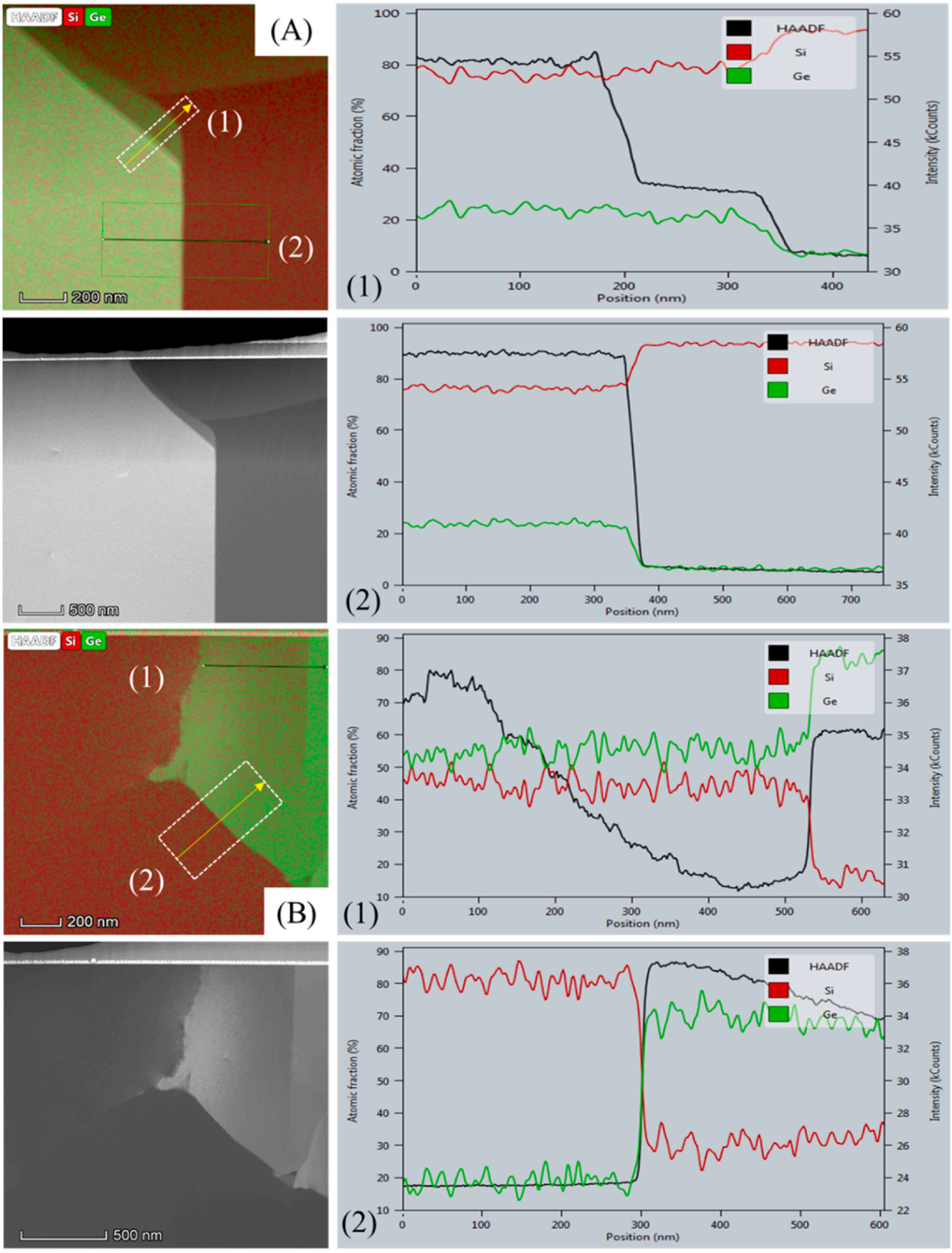

Fig. 17. TEM/EDX line scan data for (A) the crucible residue and (B) 150–106-μm fraction.

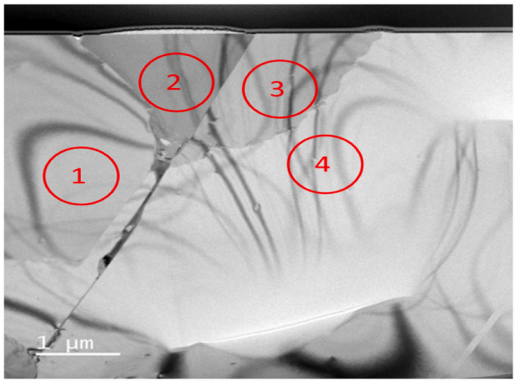

Fig. 18. Bright-field TEM image of the >850-µm fraction showing the areas of SAED analysis.

(C), respectively.

Fig. 16 presents the results of EDX line scan analysis used to quantitatively determine the Ge content of the grain-boundary region. The large Si-rich grain (red, ~0.5 µm wide) located on the far right of the image has a Ge content of 5 at%, consistent with the SEM/EDX results and a previous report [7]. Upon moving from right to left, one observes a transition to an intermediate Ge-rich grain-boundary region (red/green, 25 at% Ge, 3.5–1.55 µm), Ge-rich grain boundary (green, 67–68 at% Ge, 1.55–0.55 µm), and another intermediate Ge-rich (red/green, 20 at% Ge, ~0.6 µm wide) phase. All these transitions are accompanied by step changes in contrast. Interestingly, the three regions with high and intermediate Ge contents of 20, 25, and 67–68 at% Ge fit simple integer composition ratios i.e. Ge:Si = 1:4, 1:3, and 2:1, which indicates the formation of stoichiometric compound-like regions rather than the continuous graduation in Ge content expected based on the phase diagram.

TEM/EDX line scan analysis was also applied to the crucible residue and the 150–106-µm fraction to determine the influence of the cooling rate on the above behaviour. Fig. 17 shows the EDX traces recorded across the grain-boundary regions of these samples. In both cases, qualitatively similar behaviour was observed, namely regions of approximately constant composition transitioning to adjacent regions via a step change. However, the principal difference revealed by this analysis is that with the increasing cooling rate, the maximum Ge content of a given region markedly increased, with the most Ge-rich region in the crucible residue having a Ge content of only 25 at% (with 5 at% Ge also measured). In contrast, the 150–106-µm fraction featured a maximum Ge content of 85 at% (with 20, 55, and 70 at% Ge also measured). This behaviour suggested that the preferred stoichiometries across the samples appear to be multiples of 5 at% Ge, e.g., 5, 20, 25, 55, 70, and 85 at% Ge.

3.7. SAED patterns

Given the apparent formation of compound-like stoichiometric regions and chemical ordering observed for several stoichiometric compounds, we analysed such regions in Fig. 18 by TEM and indexed the corresponding SAED patterns using the SingleCrystal software (Fig. 19). In a diamond cubic structure, which is typical of both elemental Si and Ge, the allowed reflections are {*hkl*} all odd and {*hkl*} all even provided that $h + k + l = 4n$.

Fig. 19 shows that all regions in the examined sample had the same diamond cubic structure as their constituent elements. Moreover, we found evidence supporting the formation of atomic-scale ordered structures in the Ge-rich regions of the grain boundaries (regions 1, 2, & 3 – not shown), namely superlattice spots corresponding to not allowed reflections ([200], $[\bar{2}00]$, [600] and $[\bar{6}00]$ in the case of region 1, Ge_1Si_4; and $[\bar{2}22]$ and $[2\bar{2}2]$ in the case of region 2, Ge_2Si). Conversely, region 4, the most Si-rich region with a composition of Si–5 at% Ge, did not display such superlattice spots and therefore did not appear to be chemically ordered.

In summary, the SAED results confirmed that the Ge-rich stoichiometric regions were chemically ordered, while the Si-rich regions typical of the large bulk grains were not. This result was contrary to that reported by Hussain, et al. [7], who did not observe chemical ordering.

4. Discussion

Based on the phase diagram in Fig. 1, we expected the solidification of the SiGe system to result in strong partitioning and, hence, large but continuous chemical composition gradients across the grain-boundary region. However, the evidence presented here, including the results of SEM, XRD and TEM analyses, suggests that although strong partitioning indeed takes place, it affords regions with fixed compositions separated by compositional step changes. This behaviour is consistent with the observations of Hussain, et al. [7].

In SEM backscatter images, these discrete compositions are manifested by a microstructure with a variety of discrete grey levels, with EDX line scan data confirming that these discrete grey levels correspond to discrete compositions. In XRD analysis, these discrete compositions manifest themselves as peak splitting. The Gaussian deconvolution of these peaks yields four signals corresponding to dominant compositions, although the signal of the most Ge-rich composition is only visible for the high-angle reflections of the drop-tube samples. Given that XRD simultaneously samples multiple particles/grains, the discretisation of the Ge content should be ubiquitous across the material and cannot be the result of sampling bias due to the small field of view in the SEM analysis. Notably, the more Ge-rich compositions observed by SEM were not detected by XRD, presumably because of their low volume fractions.

The results of TEM analysis present the most compelling evidence for compositional discretisation, particularly in the Ge-rich grain-boundary regions, revealing regions with a step change in composition at what is potentially an atomically sharp interface. Moreover, most of the compositions observed by TEM appear to be multiples of 5 at% Ge (i.e., regions with 5, 20, 25, 55, 65, 70, and 85 at% Ge). Interestingly, the composition step change observed in the grain-boundary region is often >>5 at%. For instance, Fig. 16 shows a step change from 20 to 65 at% Ge, despite the observation of intermediate compositions of 25 and 55 at % Ge elsewhere. Similarly, Fig. 17 shows a step change from 55 to 85 at % Ge, despite the proximity of regions with 70 at% Ge.

The second unexpected finding is the increase in the degree of inhomogeneity with the increasing cooling rate, which contradicts the general notion that rapid solidification improves the homogeneity of as-solidified alloys. This behaviour is scientifically noteworthy but does not contribute to enhanced thermoelectric performance. Hence, no thermoelectric testing data are included in this paper. In general, rapid solidification should result in greater homogeneity [15,16], primarily by inducing solute trapping [30], whereby the partition coefficient tends to unity at high growth velocities. Moreover, the isomorphous nature of the SiGe phase diagram means that T_0 (T_0 is a temperature at which the molar free energies of the liquid and solid phases are equal), and hence, partitionless solidification should be particularly easy to access [31]. According to Mullis, et al. [32] and Nan and Bing-Bo [33], drop-tube-processed high-melting-point materials with particle sizes of 75–53 µm should achieve an undercooling of 300–350 K. The data of Panofen and Herlach [16] for Si–10 at% Ge (i.e. Si–22.3 wt% Ge) suggest that this should result in a growth velocity of ~10 m s^{-1} (cf. the diffusive speed of 2.5 m s^{-1} in SiGe estimated by the same authors). As such, the absence of solute trapping in these samples is unexplained. Moreover, even the complete absence of solute trapping would not account for the increase in inhomogeneity with the increasing driving force.

This increased inhomogeneity is manifested by SEM and TEM data. In the case of SEM, the results of point EDX measurements performed for

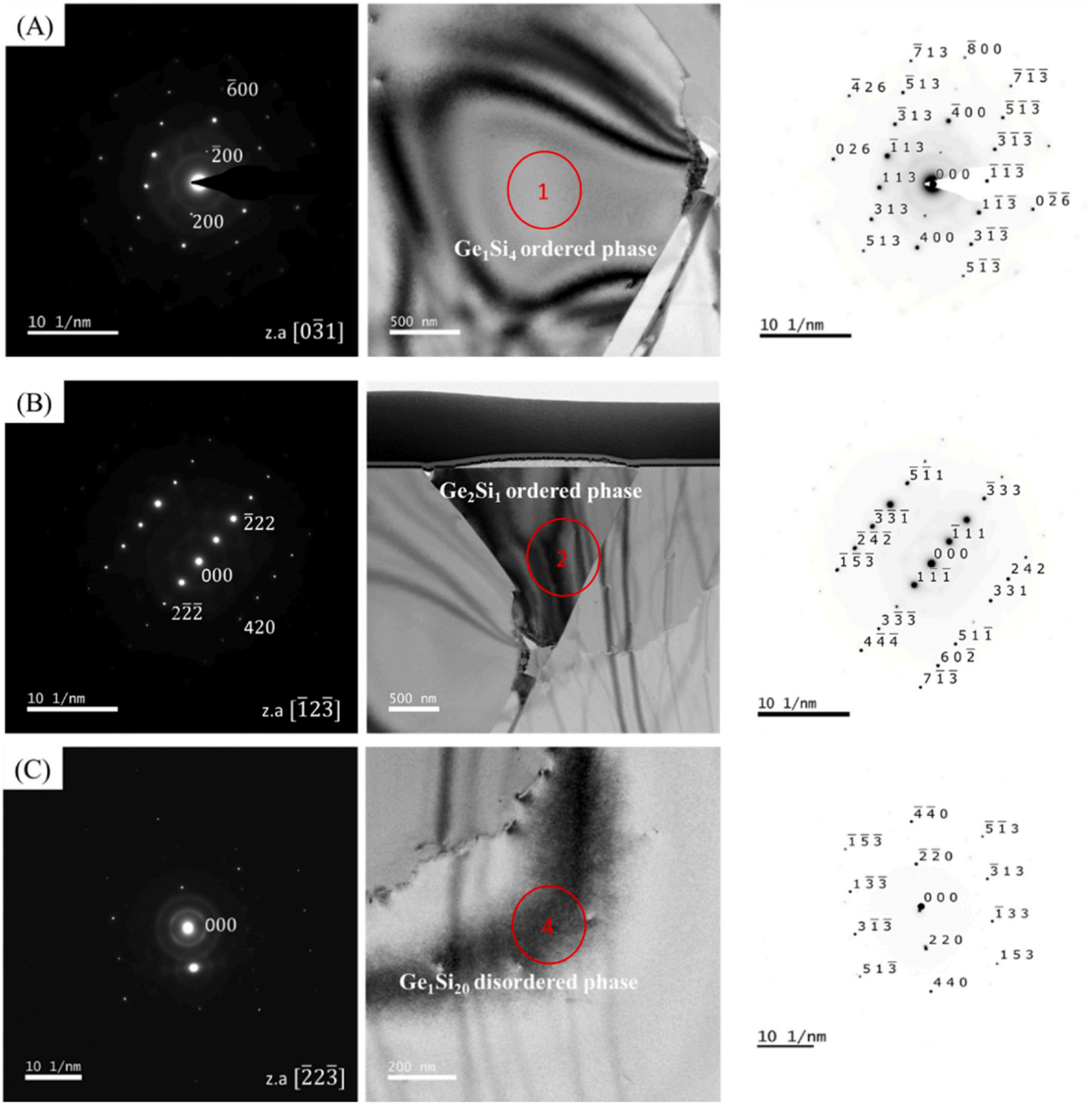

Fig. 19. Selected area electron diffraction patterns of (A, B) ordered structures in (A) region 1 (SiGe – intermediate region) and (B) region 2 (Ge-rich region) and (C) disordered structure in region 4 (Si-rich region).

the Ge-rich grain-boundary regions indicate an increase in Ge content with the increasing cooling rate. The analysis of backscatter images across all size fractions shows that the volume fraction of the bright grain-boundary material systematically decreases with the increasing cooling rate, with mass-balance calculations showing a commensurate increase in the Ge content of the grain-boundary regions. This behaviour is particularly highlighted by the comparison of the starting material (typical grain-boundary volume ≈ 37%, equivalent to 40 wt% Ge at the grain boundary) with the drop-tube powders (12–21 vol% grain boundaries, equivalent to 55–80 wt% Ge at the grain boundary). In the case of TEM, this behaviour manifests itself in the stoichiometric Ge-rich regions at the grain boundaries becoming more Ge-rich at higher cooling rates. This information is summarised in Fig. 20, which shows the TEM/EDX-determined Ge contents of the Si-rich (red), intermediate (red/green), and Ge-rich regions (green) in Figs. 16 and 17. Note that (i) the Si-rich regions are those at the grain boundaries, which are still more Ge-rich than the Si-rich bulk grains, and (ii) the error bars are based on the standard error of the measured atomic content of Ge and are representative of the variability in the Ge content distribution. The above figure reveals that regions with higher Ge contents at the grain boundaries are observed at higher cooling rates.

The results of TEM analysis indicate the formation of chemically ordered phases in the more Ge-rich regions, with superlattice spots observed for some of these regions (Fig. 19). This finding is inconsistent with the accepted view of the SiGe system as a random solid solution across the whole composition range and is contrary to the findings of

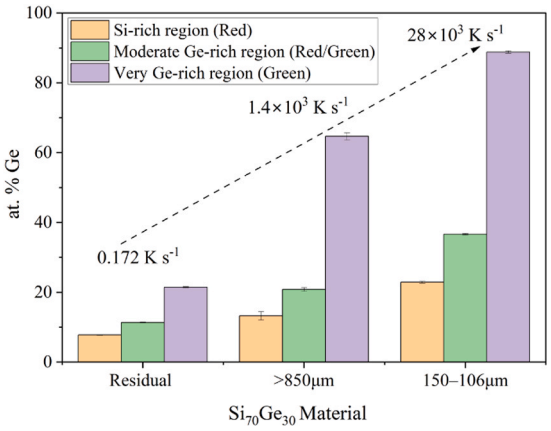

Fig. 20. Ge distribution in different samples as a function of cooling rate.

Hussain, et al. [7]. As such, the Ge-rich regions within the structure look more akin to conventional stoichiometric compounds, albeit simple chemical ordering in a single diamond cubic unit cell of eight atoms could not result in the observed range of stoichiometries, which are largely multiples of 5 at% Ge (i.e. 20 atoms, or multiples thereof, per unit cell). This suggests the occurrence of long-range (superstructural) ordering. Interestingly, Németh, et al. [34] reported the possibility of five-fold rotational symmetry in diamond nanocrystals, wherein a superstructure of 40 atoms (five unit cells) could facilitate stoichiometries that are multiples of 5 at% Ge.

According to Araki, et al. [35], strain-enhanced diffusion can facilitate ordering in the SiGe system, with strain energy promoting the formation of stable ordered structures. Müllers et al. [36] observed such ordering in strained $Si_{1-x}Ge_x$ layers grown by molecular beam epitaxy. Given the 4.24% lattice mismatch between Si and Ge, the severe segregation of Ge to grain-boundary regions during solidification may induce the accumulation of considerable strain at grain boundaries. We postulate, albeit somewhat tentatively, that the step-mediated segregation observed in the SiGe system serves as a mechanism for strain energy minimisation. That is, the total strain energy of the system is reduced via the formation of regions with uniform compositions separated by compositional step changes rather than via the formation of a continuous composition and, hence, a strain gradient across the grain boundary. Moreover, this mechanism explains the increase in the Ge content of Ge-rich regions with the increasing cooling rate by the concomitant decrease in the time available for strain relaxation and the resulting formation of larger concentration steps. Given the difficulty of preventing the segregation of Ge to the grain boundaries during solidification, the designers of thermoelectric materials should aim to utilise the above compositional discretisation to enhance the performance of SiGe materials, possibly by reducing thermal conductivity through the enhancement of phonon scattering at grain boundaries.

5. Conclusions

The rapid solidification of the Si–14.2 at% Ge (30 wt% Ge) thermoelectric alloy resulted in the severe segregation of Ge to the grain-boundary regions, which manifested itself as a series of stoichiometric regions with uniform composition separated by compositional step changes. The formation of these SiGe pseudocompounds was inconsistent with the accepted thermodynamic description of the SiGe system as a continuous random solid solution over the whole composition range.

Unlike that in nearly all other alloy systems, the degree of inhomogeneity in the as-solidified product increased upon rapid solidification. The Ge content of the most Ge-rich regions increased with the increasing cooling rate, reaching 90 at% Ge. This behaviour strongly suggested the absence of solute trapping, despite the potentially large undercooling achieved. The reason for this is currently unclear.

TEM/SAED analysis indicated that most Ge-rich regions were chemically ordered, as follows from the observation of superlattice spots. However, this was not the case for bulk Si-rich grains. Interestingly, most of the stoichiometries had compositions that were multiples of 5 at% Ge, which could not be explained by simple chemical ordering within a single diamond cubic unit cell and therefore suggested superstructural ordering. Strain-enhanced diffusion may explain some of these observations and should be investigated further for this system.

CRediT authorship contribution statement

Osama Al-Jenabi: Writing – original draft, Validation, Methodology, Investigation, Data curation, Conceptualization. **Zabeada Aslam:** Investigation. **Robert F. Cochrane:** Supervision, Resources, Methodology, Conceptualization. **Andrew M. Mullis:** Writing – review & editing, Supervision, Resources, Methodology, Data curation, Conceptualization.

Declaration of Competing Interest

The authors declare that they have no known competing financial interests or personal relationships that could have appeared to influence the work reported in this paper.

Data Availability

The raw/processed data required to reproduce these findings cannot be shared at this time due to technical or time limitations.

Acknowledgements

Osama Al-Jenabi would like to thank the Republic of Iraq, Ministry of Higher Education and Scientific Research, University of Anbar for financial support (grant no. F.A.\5940:30/11/2020). The authors gratefully acknowledge LEMAS for support & assistance.

Appendix A. Supporting information

Supplementary data associated with this article can be found in the online version at doi:10.1016/j.jallcom.2024.174560.

References

[1] J. Luo, Q. Li, J. Pei, J. Huang, Z. Li, L. Liu, Interface and surface segregation of germanium in the SiGe semiconductor, Surf. Sci. 742 (2024) 122449, https://doi.org/10.1016/j.susc.2023.122449.
[2] A.A. Khan, C. Reichel, P. Molina, L. Friedrich, D.M. Subasi, H. Neuhaus, S. Nold, Global warming potential of photovoltaics with state-of-the art silicon solar cells: influence of electricity mix, installation location and lifetime, Sol. Energy Mater. Sol. Cells 269 (2024) 112724, https://doi.org/10.1016/j.solmat.2024.112724.
[3] P.-t Chiang, S.-m Hu, W.-T. Yen, H.-J. Wu, H.-P. Hsu, C.-w Lan, A study of iron-doped SiGe growth for thermoelectric applications, J. Alloy. Compd. 967 (2023) 171700, https://doi.org/10.1016/j.jallcom.2023.171700.
[4] S. Kikuoka, R. Kanesawa, M. Yamada, K. Hamaya, K. Sawano, Enhancement of room temperature electroluminescence from strained SiGe/Ge(111) multiple quantum wells light emitting diodes, Mater. Sci. Semicond. Process. 176 (2024) 108299, https://doi.org/10.1016/j.mssp.2024.108299.
[5] C.R. Ascencio-Hurtado, A. Torres, R. Ambrosio, M. Moreno, J. Álvarez-Quintana, A. Hurtado-Macías, N-type amorphous silicon-germanium thin films with embedded nanocrystals as a novel thermoelectric material of elevated ZT, J. Alloy. Compd. 890 (2022) 161843, https://doi.org/10.1016/j.jallcom.2021.161843.
[6] N.V. Morozova, I.V. Korobeinikov, N.V. Abrosimov, S.V. Ovsyannikov, Controlling the thermoelectric power of silicon–germanium alloys in different crystalline phases by applying high pressure, CrystEngComm 22 (33) (2020) 5416–5435, https://doi.org/10.1039/D0CE00672F.
[7] N. Hussain, A.M. Mullis, N. Haque, Effect of cooling rate on the microstructure of rapidly solidified SiGe, Mater. Charact. 154 (2019) 377–385, https://doi.org/10.1016/j.matchar.2019.06.014.
[8] R. Basu, A. Singh, High temperature Si–Ge alloy towards thermoelectric applications: A comprehensive review, Mater. Today Phys. 21 (2021) 100468, https://doi.org/10.1016/j.mtphys.2021.100468.

[9] B. Cook, Silicon–germanium: the legacy lives on, Energies 15 (8) (2022) 2957, https://doi.org/10.3390/en15082957.
[10] H. Lai, Y. Peng, J. Gao, M. Kurosawa, O. Nakatsuka, T. Takeuchi, L. Miao, Silicon-based low-dimensional materials for thermal conductivity suppression: Recent advances and new strategies to high thermoelectric efficiency, Jpn. J. Appl. Phys. 60 (SA) (2020) SA0803, https://doi.org/10.35848/1347-4065/abbb69.
[11] D. Narducci, F. Giulio, Recent advances on thermoelectric silicon for low-temperature applications, Materials 15 (3) (2022) 1214, https://doi.org/10.3390/ma15031214.
[12] R. Basu, A review on single crystal and thin film Si–Ge alloy: growth and applications, Mater. Adv. 3 (11) (2022) 4489–4513, https://doi.org/10.1039/D2MA00104G.
[13] R. Freer, A.V. Powell, Realising the potential of thermoelectric technology: A Roadmap, J. Mater. Chem. C. 8 (2) (2020) 441–463, https://doi.org/10.1039/C9TC05710B.
[14] H. Nagai, Y. Nakata, H. Minagawa, K. Kamada, T. Tsurue, M. Sasamori, T. Okutani, Synthesis of Si–Ge alloy by rapid cooling in short-duration microgravity, Jpn. J. Appl. Phys. 41 (2R) (2002) 749, https://doi.org/10.1143/jjap.41.749.
[15] P. Zhang, Z. Wang, H. Chen, H. Yu, L. Zhu, X. Jian, Effect of cooling rate on microstructural homogeneity and grain size of n-Type Si-Ge thermoelectric alloy by melt spinning, J. Electron. Mater. 39 (2010) 2251–2254, https://doi.org/10.1007/s11664-010-1314-1.
[16] C. Panofen, D. Herlach, Solidification of highly undercooled Si and Si–Ge melts, Mater. Sci. Eng.: A 449 (2007) 699–703, https://doi.org/10.1016/j.msea.2006.02.443.
[17] D.M. Herlach, D. Simons, P.-Y. Pichon, Crystal growth kinetics in undercooled melts of pure Ge, Si and Ge–Si alloys, Philos. Trans. R. Soc. A: Math., Phys. Eng. Sci. 376 (2113) (2018) 20170205, https://doi.org/10.1098/rsta.2017.0205.
[18] D. Li, K. Eckler, D. Herlach, Evidence for transitions from lateral to continuous and to rapid growth in Ge-1at% Si solid solution, Europhys. Lett. 32 (3) (1995) 223, https://doi.org/10.1209/0295-5075/32/3/006.
[19] D. Li, D. Herlach, Containerless solidification of germanium by electromagnetic levitation and in a drop-tube, J. Mater. Sci. 32 (1997) 1437–1442, https://doi.org/10.1023/A:1018593615171.
[20] S. Battersby, R. Cochrane, A. Mullis, Growth velocity-undercooling relationships and microstructural evolution in undercooled Ge and dilute Ge-Fe alloys, J. Mater. Sci. 34 (1999) 2049–2056, https://doi.org/10.1023/A:1004547423857.
[21] L. Tayebi, Z. Zamanipour, M. Mozafari, P. Norouzzadeh, K.F. Ede, J.S. Krasinski, D. Vashaee, Differential Thermal Analysis of Nanostructured Si0. 80Ge0. 20 Thermoelectric Material. 2012 IEEE Green Technologies Conference, IEEE, 2012, https://doi.org/10.1109/green.2012.6200977.
[22] Z. Zamanipour, E. Salahinejad, P. Norouzzadeh, J.S. Krasinski, L. Tayebi, D. Vashaee, The effect of phase heterogeneity on thermoelectric properties of nanostructured silicon germanium alloy, J. Appl. Phys. 114 (2) (2013), https://doi.org/10.1063/1.4813474.
[23] J.C. Duda, T.S. English, D.A. Jordan, P.M. Norris, W.A. Soffa, Controlling thermal conductivity of alloys via atomic ordering, J. Heat. Transf. 134 (1) (2012), https://doi.org/10.1115/1.4004843.
[24] O. Oloyede, T.D. Bigg, R.F. Cochrane, A.M. Mullis, Microstructure evolution and mechanical properties of drop-tube processed, rapidly solidified grey cast iron, Mater. Sci. Eng.: A 654 (2016) 143–150, https://doi.org/10.1016/j.msea.2015.12.020.
[25] E. Takasuka, E. Tokizaki, K. Terashima, S. Kimura, Direct measurement of spectral emissivity of liquid Si in the range of visible light, Appl. Phys. Lett. 67 (2) (1995) 152–154, https://doi.org/10.1063/1.114650.
[26] E. Takasuka, E. Tokizaki, K. Terashima, S. Kimura, Emissivity of liquid germanium in visible and near infrared region, J. Appl. Phys. 82 (5) (1997) 2590–2594, https://doi.org/10.1063/1.366071.
[27] M. Alias, N. Rammo, M. Makadsi, Lattice parameter and density of Ge–Si solid solutions, Renew. Energy 24 (3-4) (2001) 347–351, https://doi.org/10.1016/S0960-1481(01)00015-5.
[28] B. Nasiri-Tabrizi, Thermal treatment effect on structural features of mechano-synthesized fluorapatite-titania nanocomposite: A comparative study, J. Adv. Ceram. 3 (1) (2014) 31–42, https://doi.org/10.1007/s40145-014-0090-4.
[29] V. Shah, A. Dobbie, M. Myronov, D.R. Leadley, Reverse graded SiGe/Ge/Si buffers for high-composition virtual substrates, J. Appl. Phys. 107 (6) (2010), https://doi.org/10.1063/1.3311556.
[30] M.J. Aziz, T. Kaplan, Continuous growth model for interface motion during alloy solidification, Acta Metall. 36 (8) (1988) 2335–2347.
[31] D.M. Herlach, Non-equilibrium solidification of undercooled metallic melts, Metals 4 (2) (2014) 196–234, https://doi.org/10.3390/met4020196.
[32] A.M. Mullis, O.E. Jegede, T.D. Bigg, R.F. Cochrane, Dynamics of core–shell particle formation in drop-tube processed metastable monotectic alloys, Acta Mater. 188 (2020) 591–598, https://doi.org/10.1016/j.actamat.2020.02.017.
[33] W. Nan, W. Bing-Bo, Droplet undercooling during containerless processing in a drop tube, Chin. Phys. Lett. 21 (6) (2004) 1120, https://doi.org/10.1088/0256-307x/21/6/040.
[34] P. Németh, K. McColl, L.A. Garvie, C.G. Salzmann, M. Murri, P.F. McMillan, Complex nanostructures in diamond, Nat. Mater. 19 (11) (2020) 1126–1131, https://doi.org/10.1038/s41563-020-0759-8.
[35] T. Araki, N. Fujimura, T. Ito, Mechanism for ordering in SiGe films with reconstructed surface, Appl. Phys. Lett. 71 (9) (1997) 1174–1176, https://doi.org/10.1063/1.119617.
[36] E. Müllers, H.-U. Nissen, K. Mäder, M. Ospelt, H. Von Känel, Occurrence of two ordered structures in Si–Ge systems, Philos. Mag. Lett. 64 (4) (1991) 183–189, https://doi.org/10.1080/09500839108214541.